Experiments on In-Channel Swimming of an Untethered Biomimetic Robot with Different Helical Tails

Ahmet Fatih Tabak, *Student Member, IEEE*, Serhat Yesilyurt, *Member, IEEE*

***Abstract*—Experiments are carried out with a cm-scale biomimetic swimming robot, which consists of a body and a rigid helical tail and mimics typical eukaryotic micro organisms, inside circular channels filled with viscous fluids. The body of the robot is made of a cylindrical capsule, which includes an on-board power supply, a dedicated DC-motor, and a driving circuitry with IR-receiver for remote control purposes. In experiments geometric parameters of the helical tail, wavelength and amplitude, and the diameter of the circular channels are varied to understand the effect of those parameters on the swimming speed of the robots. Models, based on slender body theory (SBT) and resistive force theory (RFT), are implemented to predict the swimming speeds, which are then compared with experimentally measured values. A simple model for the DC-motor dynamics is included to account for the contact friction effects on the body rotation rates. Model results agree reasonably well with experimental measurements.**

I. Introduction

EXPERIMENTS recently conducted on bio-inspired actuation mechanisms manifest encouraging progress on medical applications of micro swimming robots, which offer revolutionary improvements in minimal invasive surgery and other therapeutic practices [1,2,3,4]. Honda *et al.* [5] demonstrated the swimming of an untethered bio-inspired swimmer with a helical tail, which is rotated by external rotating magnetic fields, inside a channel. Zhang *et al.* [6,7] studied the effect of applied magnetic field and payload geometry on the velocity of a magnetically actuated helical microfilament, which is constructed by means of IC-manufacturing techniques and activated by Helmholtz coil pairs. Chen *et al.* [8] studied maneuverability of a cm-scale bio-inspired robot with four independent DC-motors actuating four rigid helical tails. Peyer *et al.* [9] and authors [10] studied the effect of near-solid-boundaries and channel walls on the motion and trajectories of the swimmer robot. Mahoney *et al.* [11] presented experimental results of the velocity control study on a magnetically driven helical robot with gravity compensation.

Scallop theorem suggests that the fluid friction acting on a self-propelling body in micro scales at small Reynolds numbers ($Re < 0.1$) is significantly dominant to inertial forces [12,13]. Gray and Hancock [14] articulated a linear relationship between hydrodynamic forces acting on bacterial flagella and their structural deformation based on local resistance coefficients, also known as resistive force theory (RFT). Brennen and Winet [15] listed a modified coefficient set for finite-length cylinders in motion near plane boundaries. Sir James Lighthill [16] presented approximate asymptotical results for swimming of an organism with a helical tail and a spherical body based on the slender body theory (SBT). Chattopadhyay and Wu [17] compared the time-averaged velocity results obtained from boundary element method, from slender body theory and from resistive force theory against experimental measurements.

Higdon and Muldowney [18] studied the effect of proximity to channel walls on fluid resistance acting on moving micron-sized spherical particles by means of CFD simulations and lubrication solutions. Lauga *et al.* [19] used the resistance matrix approach to determine the effective fluid drag on self-propelling swimmers undergoing 6-dof rigid body motion near solid boundaries. Felderhof [20] studied the effect of wave propagation on forward translation of small bodies in viscous domains, which are confined by narrow channels, based on the perturbation solutions provided by Happel and Brenner [21]. Lauga and Powers [22] provided an extended review on the swimming of micro organisms and bio-inspired artificial mechanisms.

In this study we manufactured a biomimetic untethered helical robot comprised of a capsule attached to a replaceable rigid helical tail of arbitrary geometric properties. A commercially available cm-scale rechargeable battery pack is embedded in the swimmer's body as an on-board power supply to ensure on-line actuation and control. Helical wave propagation is carried out by a coreless brushed DC-motor, which is on-off controlled by an IR transducer.

We parameterized the helical wave geometry and conducted experiments with a number of different body-tail assemblies. Open-ended cylindrical glass channels of two different diameters are used to confine the environment of the biomimetic robot, which is completely submerged in a viscous oil to ensure low Reynolds number swimming conditions of micro swimming robots in aqueous solutions. Rigid body translation of the biomimetic robot, which is observed to be limited with the symmetry axis of the channel due to its weight, is captured by a CCD-camera located atop.

A hydrodynamic model of the swimming robot is implemented to predict time-averaged forward velocity of the swimmer and its body rotation rate based on the slender body theory given by [16]. Moreover another time-dependent model is implemented with the incorporation DC-

Manuscript received April 28, 2012. This work was supported in part by the Scientific and Technological Research Council of Turkey under Grant 111M376 (T.A.CF-12-00867).

Authors are with the Faculty of Engineering and Natural Sciences, Sabanci University, Orhanli Tuzla, 43956 Istanbul, Turkey

(e-mail: tabak@sabanciuniv.edu, syesilyurt@sabanciuniv.edu).

motor dynamics to account for the contact friction, resistive force theory and the resistance matrix approach, which is demonstrated, e.g. in [19], in order to obtain time-dependent translational and rotational velocity of the swimmer. Time-averaged numerical and experimental results are compared to identify the effects of channel walls and wave geometry on swimmer's hydrodynamic behavior.

II. Methodology

A. Biomimetic Robot Design and Experimental Setup

Biomimetic swimmer robot is comprised of two links, which are the body and the tail and joined with a revolute joint. Right-handed helix-shaped rigid tail is manufactured by winding a 1-mm-diameter copper wire into a coil around a smooth cylinder of a certain diameter for uniform amplitude, followed by stretching evenly in order to form identical waves throughout. Actual length of the wire varies with the wave geometry but length of the helix is fixed at 60 mm. One end of the rigid tail is deformed with a steep hyperbolic tangent profile and inserted into the mechanical coupling and clamped by two setscrews. In total, sixteen helical tails with different wave geometries are manufactured.

Mechanical coupling is manufactured out of an aluminum alloy and has two grooves in order to transmit the mechanical power from DC-motor to the tail. Coreless brushed DC-motor is housed in the plastic seal astern the body as depicted in Fig. 1a. Power leads of the motor are secured within the 0.75 mm thick cylindrical silica-glass cover, which has a hemispherical surface to the fore, while its rotor is fitted tightly into the mechanical coupling forming the revolute joint as indicated in Fig. 1a. DC-motor is driven by a 400 kHz PWM voltage controller circuit including an IR-receiver. Driver circuitry and the DC-motor, which are discussed in detail in Section II-*B*, are powered by a single-cell rechargeable 3.7 V 70 mA·h Li-Po battery pack.

Untethered biomimetic robot is placed inside constant-cross-section glass tubes with open ends as depicted in Fig. 1b. It is also noted that the long axis of the tails and symmetry axis of the channels are parallel to the **x**-axis of the lab frame. Furthermore, glass tubes of 350 mm in length with different inner diameters are sitting stationary ot the bottom of the silicone oil tank while fully submerged. Physical properties of the silicone oil are measured as $\rho = 985$ kg/m^3 and $\mu = 3.5$ Pa·s.

Helical wave propagation is on-off controlled by an external IR remote controller, i.e. 'on' being full throttle and 'off' being zero motor-current. Swimming of the autonomous robot inside the glass tube is captured by a CCD-camera, which samples 640-by-480 pixels at a rate of 30 fps, placed 15 cm above the tank as depicted in Fig. 2a. Eight symmetrically coded stripes of four different colors placed on the side of the plastic seal as shown Fig. 2b in order to determine the body rotation rates. Complete list of parameters of the biomimetic robot and the experimental setup are presented in Table I.

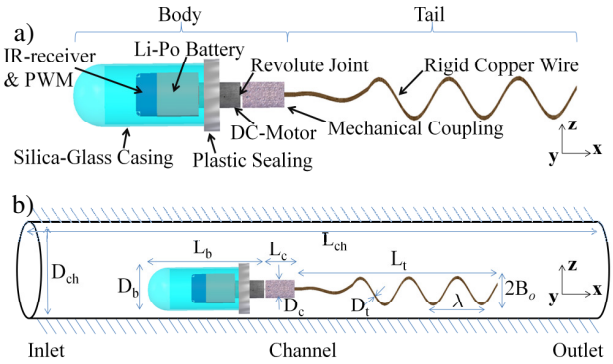

Fig. 1. a) Biomimetic robot assembly; b) Robot inside the channel presented with geometric parameters.

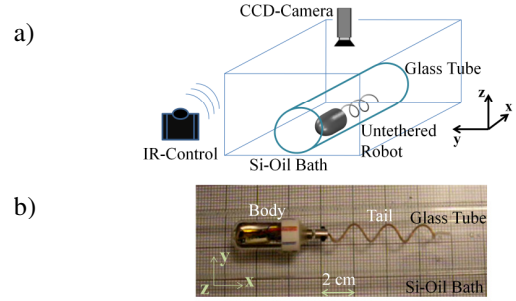

Fig. 2. a) Components of experimental setup; b) Camera view of cm-scale biomimetic robot confined to glass channel.

TABLE I
BIOMIMETIC ROBOT AND EXPERIMENTAL SETUP

D_{ch}	Channel Diameter	40 mm (Wide); 30 mm (Narrow)
L_{ch}	Channel Length	350 mm
D_b	Body Diameter	18 mm
L_b	Body Length	35 mm
D_c	Coupling Diameter	6 mm
L_c	Coupling Length	10 mm
L_t	Helix Length	60 mm
D_t	Copper Wire Diameter	1 mm
B_o	Wave Amplitude	Parameterized (See Fig. 5-6)
λ	Wave Length	Parameterized (See Fig. 5-6)
-	Body-Coupling Mass	10.7 g
-	DC-motor Diameter	6 mm
-	DC-motor Length	11 mm
-	Rotor Diameter	0.8 mm
-	Li-Po Battery Volume	5.5 mm x14mm x17mm
ρ	Si-Oil Density	985 kg/m^3
μ	Si-Oil Viscosity	3.5 Pa·s
-	CCD-Camera	640-by-480 Pixels @ 30 fps
-	CCD-Camera Elevation	150 mm

B. Mathematical Model

1) Slender Body Theory (SBT): Lighthill [16] presented an SBT-based approach to determine the time-averaged forward translation rate U_x and the time-averaged body rotation rate Ω_x of swimmers with helical tails, such eukaryotic as micro organisms, as follows:

$$U_x = \lambda C_U \left(1-\alpha^2\right)\left[-1-\log(\varepsilon)+A_1(\alpha)\right]\chi\omega \Big/ 2\pi \quad (1)$$

$$\Omega = 4\pi\mu B_o^2 \omega \chi C_\Omega L_t / E_x \quad (2)$$

$$\chi = 1\Big/\left[-(1-\alpha^2)-\left(2-\alpha^2\right)\log(\varepsilon) + \alpha^2 A_1(\alpha)+2\left(1-\alpha^2\right)A_2(\alpha)\right] \quad (3)$$

$$C_U = 1/\left(1 + 0.5 D_x \psi \mathrm{D_b}/\mathrm{L_t}\right) \tag{4}$$

$$C_\Omega = \left(1 + 0.5 D_x \Psi\, \mathrm{D_b}/\mathrm{L_t}\right) C_U \tag{5}$$

$$\Psi = 1.5\Big[2 - \alpha^2 - 3\alpha^{-1} + 2\alpha^{-1}\log\left(k\mathrm{L_t}\right) - \left(1+\alpha^2\right)\log\left(\varepsilon\right) - 2\mathrm{A}_3\left(\alpha\right) - \left(1-\alpha^2\right)\mathrm{A}_1\left(\alpha\right)\Big] \tag{6}$$

$$\psi = \Psi - 1.5\alpha^2\left(1-\alpha^2\right)\left[-1 - \log\left(\varepsilon\right) + \mathrm{A}_1\left(\alpha\right)\right]^2 \chi \tag{7}$$

where α is the ratio of apparent length to actual length of the tail, ω is the tail actuation frequency, D_x and E_x are the translational and rotational drag coefficients of the swimming robot's body along the **x**-axis respectively, ε=2.6αD$_t$/λ , and k=2π/λ . Here, A$_{\{1,2,3\}}$ are periodic integrals of the flow fields signified by local Stokeslet functions throughout the tail, χ is the dimensionless helix torque, Ψ and ψ are velocity reduction functions, C_U and C_Ω are translation and rotation rate corrections. Exact forms of the integrals, A$_{\{1,2,3\}}$, can be found in [16].

Fluid resistance formulae for translation and rotation of a spheroid bodies in arbitrary directions and near solid boundaries are presented extensively in literature based on the ratio of its semi-axes, and near-wall proximity [18, 20, 21, 24, 25, 26]. Resistance coefficients D_x and E_x used in this work are presented by Perrin [26] for prolate spheroids submerged in unbounded viscous fluids.

2) Resistive Force Theory (RFT) model: Time-dependent trajectory of a two-link swimming microrobot with six degrees-of-freedom is solved by the equation of motion with hydrodynamic forces determined by the resistance relationships according to the RFT as follows:

$$\mathcal{F}_\mathrm{b} + \mathcal{F}_\mathrm{t} + \mathcal{F}_{eff} = 0\,, \tag{8}$$

$$\mathcal{F}_\mathrm{b,t} = -\mathbf{B}_\mathrm{b,t}\mathbf{V}_\mathrm{b,t} \tag{9}$$

where $\mathcal{F}$ is the six-by-one generalized resistance force vector acting on robot surfaces, subscripts b, t and *eff* denote body, tail and effective friction respectively. Here, **V** is the generalized six-by-one rigid body velocity vector, and **B** is the six-by-six fluid resistance matrix. The contact friction force is treated separately than standard fluid resistance forces.

The position vector on the rotating right-handed helix with wavelength λ, rotation ω, and modified local amplitude for an arbitrary **x**-position, x_t, on the helix with respect to robot's center of mass in lab frame is specified by:

$$\mathbf{P} = \Big[x_\mathrm{t} \quad \mathrm{B}_o\left(1 - e^{-cx_\mathrm{t}/\mathrm{L_t}}\right)\sin\left(\omega t - kx_\mathrm{t}\right) \quad \mathrm{B}_o\left(1 - e^{-cx_\mathrm{t}/\mathrm{L_t}}\right)\cos\left(\omega t - kx_\mathrm{t}\right)\Big]' \tag{10}$$

where c is the shape constant marking the converging end of the helix, which is set to 100.

Rotational velocity vector of a right-handed helix with respect to robot's center of mass is obtained from:

$$\frac{\mathrm{d}\mathbf{P}}{\mathrm{d}t} = \mathbf{\Omega}_\mathrm{t} \times \mathbf{P} \tag{11}$$

where the tail rotation rate vector is $\mathbf{\Omega}_\mathrm{t}$=[ω 0 0]'.

Tail resistance matrix $\mathbf{B}_\mathrm{t}$ is obtained from the integration of the local force coefficients which are projected onto the lab coordinates in the following fashion:

$$\mathbf{B}_\mathrm{t} = \int_{\mathrm{L_t}} \begin{bmatrix} \mathbf{R}\,\mathbf{C}\,\mathbf{R}' & -\mathbf{R}\mathbf{C}\,\mathbf{R}'\mathbf{S} \\ \mathbf{S}\,\mathbf{R}\,\mathbf{C}\,\mathbf{R}' & -\mathbf{S}\,\mathbf{R}\,\mathbf{C}\,\mathbf{R}'\mathbf{S} \end{bmatrix} \left(\ell/\mathrm{L_t}\right)\,\mathrm{d}x \tag{12}$$

where ℓ is the actual length of the wire, **S** is the skew-symmetric matrix corresponding to the cross product with the position vector **P**, **R** is the rotation matrix between the local Frenet-Serret coordinates **tnb** and the lab frame **xyz**, with local tangential, **t**, normal, **n**, and binormal, **b**, vectors [23] are depicted in Fig. 3.

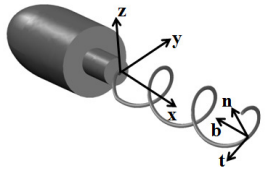

Fig. 3. Local Frenet-Serret frames (**tnb**) and lab frame (**xyz**).

The local resistance on the tail, denoted by **C** in (9), is considered as a diagonal matrix that consists of the local resistance coefficients in the tangent, binormal, and normal directions, which are given by Gray and Hancock [14] as:

$$c_t = 2\pi\mu/\left(\log\left(\lambda/\mathrm{D_t}\right) - 0.5\right) \tag{13}$$

in tangential direction, and

$$c_{n,b} = 4\pi\mu/\left(\log\left(\lambda/\mathrm{D_t}\right) + 0.5\right) \tag{14}$$

in normal and binormal directions respectively.

From (8)-(9) and separating the tail rotation rate $\mathbf{\Omega}_\mathrm{t}$ in$\mathbf{V}_\mathrm{t}$, one obtains the rate of rigid body translation **U** and the body rotation rate $\mathbf{\Omega}_\mathrm{b}$ of the swimming robot as:

$$\begin{bmatrix} \mathbf{U} \\ \mathbf{\Omega}_\mathrm{b} \end{bmatrix} = \left(\mathbf{B}_\mathrm{b} + \overline{\mathbf{B}}_\mathrm{t}\right)^{-1}\left(-\mathbf{B}_\mathrm{t}\begin{bmatrix} \mathbf{0} \\ \mathbf{\Omega}_\mathrm{t} \end{bmatrix} + \mathcal{F}_\mathrm{f}\right) \tag{15}$$

where $\overline{\mathbf{B}}_\mathrm{t}$ is the tail resistance matrix, given by (12), with the entire fourth column and fourth row set to zero given that the **x**-rotation of the helix is specified as the control input in (11).

The resistance matrix $\mathbf{B}_\mathrm{b}$ for the rigid body in (15) is generalized as follows:

$$\mathbf{B}_\mathrm{b} = \begin{bmatrix} \mathbf{D} & \mathbf{G} \\ \mathbf{G}' & \mathbf{E} \end{bmatrix} \tag{16}$$

where **D** and **E** are 3×3 diagonal matrices that correspond to translational and rotational resistances of the body, **G**, is considered non-zero if center of mass of the robot and geometric center of the body do not coincide.

Dynamics of the DC-motor, which is acting as a bacterial motor and allowing both links to rotate in counter directions [17,27], are included only in RFT-model. Instantaneous current I(t) drawn by the DC-motor is determined by the fol-

lowing differential equation for the electromechanical circuit shown in Fig. 4:

$$\mathrm{L}\frac{\mathrm{dI}(t)}{\mathrm{d}t}+\mathrm{R}(t)\mathrm{I}(t)=\mathrm{V}(t)-\mathrm{K_b}\omega_\mathrm{m} \tag{17}$$

where L is the measured motor inductance, ω_m is the total rotation rate sustained by DC-motor, and $\mathrm{K_b}$ is the measured back-emf constant of the DC-motor [28].

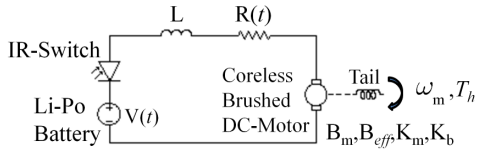

Fig. 4. Equivalent electromechanical circuit of the actuation system.

The effective torque constant B_{eff} satisfying the linear relationship between the total rotational friction acting on the robot and the total instantaneous rotation rate ω_m is given by:

$$(\mathrm{B}_{eff}+\mathrm{K_b}\mathrm{K_m}/\mathrm{R}(t))\omega_\mathrm{m}=\mathrm{V}(t)\mathrm{K_m}/\mathrm{R}(t)-T_h \tag{18}$$

Where $\mathrm{K_m}$ is the measured torque constant, and T_h is the total calculated hydrodynamic torque on the rotor whereas $\mathrm{I}(t)\mathrm{K_m}$ is the mechanical coupling torque between the rotor and the stator. It is noted that for small rotation rates, the pure rotor friction is measured to be on the order of 10^{-7}. Hence, the rotational friction in (18) is significantly dominated by the body-channel interaction. It is also noted that Eq. (18) is obtained by eliminating all moments of inertia in the equation of motion of the DC-motor [28].

Finally, the friction effect is specified as:

$$\mathcal{F}_{eff}=\begin{bmatrix}0 & 0 & 0 & -\mathrm{B}_{eff}\omega_\mathrm{m} & 0 & 0\end{bmatrix}'. \tag{19}$$

Electromechanical properties of the actuation system are listed in Table II. Battery voltage $\mathrm{V}(t)$ and equivalent resistance $\mathrm{R}(t)$ are experimentally measured to be current dependent, which are in effect coupling (17) with (8), thus DC-motor dynamics to RFT-based hydrodynamics.

III. Results

Images captured by CCD-camera are inspected frame-by-frame in order to resolve the body rotation rate, Ω_x, and tail rotation rate, ω, along with swimmer's forward velocity U_x only, given that the robot's weight is bigger in magnitude than the buoyancy force acting on it, hence, infinitesimal lateral rigid body translations or rotations are neglected. Furthermore, based on the Nyquist-rate, the sampling rate of the CCD-camera is found sufficient to resolve the swimmer rotation rates.

Results are obtained by averaging out five distinct measurements and visible error bars are calculated with 95 per cent confidence interval. Observed rotation rate of the tail is input in SBT and RFT models as the actuation frequency ω.

RFT model calculations are carried out with all rows of the resistance matrices set to zero except the first and the fourth rows in (12) and (16) to ensure the calculation of the

TABLE II
Actuation System Parameters

$\mathrm{R}(t)$	Equivalent Resistance	10.4 +30 exp(–54.6 I(t)) +exp(I(t)) –1.555 I(t) Ω
$\mathrm{V}(t)$	Battery Voltage	3.7 – 0.8 I(t) V
L	Motor Inductance	0.082 H
$\mathrm{K_m}$	Torque Constant	0.00045 N·m/A
$\mathrm{K_b}$	Back-emf Constant	0.004 V·s/rad
B_{eff}	Effective Friction	(variable) N·m·s/rad (See Fig. 5-6)
$\mathrm{B_m}$	Rotor Friction	$7\mathrm{x}10^{-7}$ N·m·s/rad @ $\omega \approx 1$ Hz
ω_m	Motor Rotation Rate	($=\omega-\Omega_x$) Hz (See Fig. 5-6)
-	Li-Po Pack Rating	70 mA·h with 3.7 V
-	PWM Frequency	400 kHz
-	IR Wave Length	930 nm

trajectory for two degrees of freedom, forward translation and body rotation. Helical tail is discretized by at least 100 intervals per wavelength. Time-integration of the model is carried out by Adams-Bashforth-Moulton PECE solver [30] and equation of motion specified by (8) and motor current given in (17) are solved for three complete periods. It is noted that each simulation took approximately two to three seconds with a 64-bit high-end linux-based workstation.

In the SBT model, body-drag coefficients D_x and E_x in (2), (4) and (5) are calibrated only once in order to compensate the shear and friction effects of the channel walls on the swimmer. Corresponding calibration constants, which are presented in Table III, are obtained by the inverse solution of the velocity kinematics (15) with observations. In the RFT-model, D_x of **D** in (16) is set exactly identical to the value that is used in SBT-study. However, E_x of **E** in (16) is used without calibration because combined effect of additional shear and friction on total rotation rate is resolved by DC-motor dynamics given by (18) in terms of effective rotational friction constant B_{eff}. The fact that identical rotational calibration being used in the SBT-model to predict both wide and narrow channels implies that untethered robot is under the influence of comparable external rotational torques for both channels.

TABLE III
Body Drag Calibrations

SBT-model	
Translational **x**-drag	1.95 D_x (Wide Ch.); 3.6 D_x (Narrow Ch.)
Rotational **x**-drag	0.6 E_x (Wide Ch.); 0.6 E_x (Narrow Ch.)
RFT-model	
Translational **x**-drag	1.95 D_x (Wide Ch.); 3.6 D_x (Narrow Ch.)
Rotational **x**-drag	1 E_x (Wide Ch.); 1 E_x (Narrow Ch.)

Sensitivity of effective rotational friction constant, B_{eff}, to wavelength, amplitude and the channel diameter is studied with only the RFT model. It is noted that translational friction between swimmer and channel surfaces requires further analysis. Motor current, $\mathrm{I}(t)$, and hydrodynamic efficiency of the biomimetic robot, η, are studied elsewhere [29].

Time-averaged RFT and experiment-based results presented here are obtained via averaging out the final two periods whereas results obtained by SBT-based approach are already time-averaged do not require further processing.

As it is presented in Fig. 5a-d and Fig. 6a-d by the time-averaged forward velocities, U_x, robots travel slower in

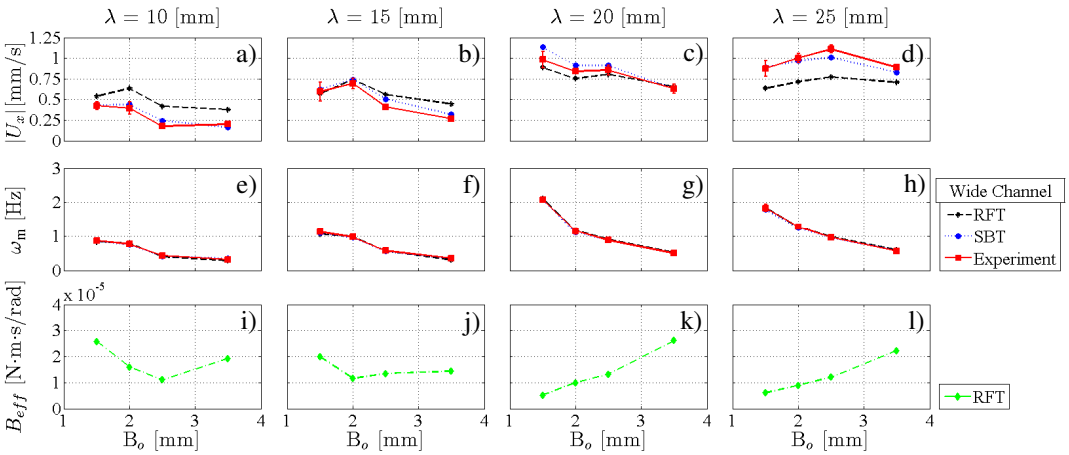

Fig. 5. Wide channel experiment results with respect to parameterized wave length and wave amplitude: a-d) time-averaged forward velocity; e-h) time-averaged motor rotation rate; i-l) time-averaged effective rotational friction constant. Re_{max} = 0.0058 with B_o = 2.5 mm and λ = 25 mm.

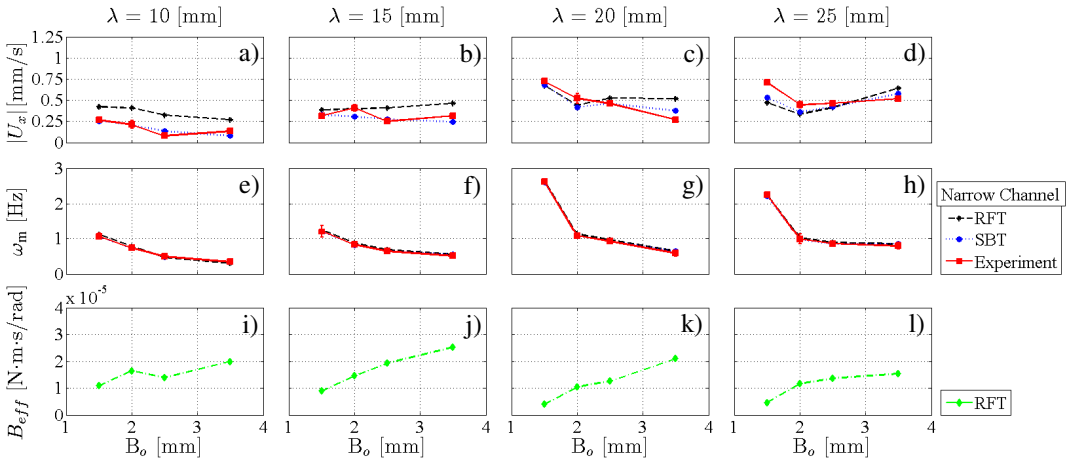

Fig. 6. Narrow channel experiment results with respect to parameterized wave length and wave amplitude: a-d) time-averaged forward velocity; e-h) time-averaged motor rotation rate; i-l) time-averaged effective rotational friction constant. Re_{max} = 0.0038 with B_o = 1.5 mm and λ = 20 mm.

narrow channels indicating that the effective fluid drag exerted on untethered robots is higher in the narrow channel than in the wide channel, assuming forward thrust is the same if not increased by traction (see Table III).

Moreover, the observed DC-motor velocity values, ω_m, are found to be identical in wide and narrow channel experiments as presented in Fig. 5e-h and Fig. 6e-h. Furthermore, different effective rotational friction constant, B_{eff}, values calculated by the RFT-model in both channels (see Fig. 5i-l and Fig. 6i-l) can be attributed to different flow field characteristics.

We suspect that surface contact occurs intermittently under the influence of the complex flow field induced by the untethered robot around the body and the tail, given the fact that each body-tail assembly has a constant individual mass. Thus smaller B_{eff} suggests longer lift-off time where lubrication effects become more important. It is also observed that B_{eff} is mostly dependent on the amplitude B_o instead of the wave length λ as depicted in Fig. 5i-l and Fig. 6i-l.

Forward velocities predicted by the SBT-model are in better agreement with the experimental results than the RFT-model results as demonstrated in Fig. 5a-d and Fig. 6a-d. Effects of the helical tail parameters are predicted with high accuracy via SBT approach with a few exceptions: In Fig. 6d it is observed that both RFT and SBT-model's calculations fail to predict the wave amplitude B_o dependency accurately for λ=25 mm. In general, forward velocity increases converging to a maximum as wave length increases, and decreases with increasing wave amplitude B_o except for the instance of λ=25 mm. The latter behavior transforms into a more complex pattern as untethered robot is placed inside the narrow channel.

Observations presented in Fig. 5e-h and Fig. 6e-h illustrate that the hydrodynamic torque required for the rotation of the body increases with the amplitude, B_o, thus total rotation rate, ω_m, values of the DC-motor decreases. On the other hand, similarly to forward velocity results, ω_m increases with the wave length converging to a maximum and saturates thereafter. It is noted that, body rotation rates are on the order of 10^{-2} to 10^{-1}. It is also noted that SBT and RFT-based calculations predict observed body rotation rates within 1 to 50 percent error; large values of error are observed with the RFT-based model.

IV. Conclusion

We built a prototype under-actuated swimming robot

mimicking bacterial propulsion with an on-board power source. Untethered swimming of the robot is confined to open-ended cylindrical glass channels fully submerged in a viscous oil reservoir. We recorded trajectories of the robot with a CCD-camera at adequate sampling rates and resolutions for conducted experiments. Swimming velocity of the robot is determined from the total traveled distance and time over grid with 2-mm-long markers in order to eliminate errors on spatial resolution. Body and tail rotation rates are obtained from frame-by-frame inspection of the position of the tail over the range of travel. Observed velocities are compared with numerical results predicted by SBT and RFT-based models.

Overall size of the robot is constrained due to available electrical components, battery pack and coreless DC-motor with enough torque to rotate the helical tail under high viscous load. Although the prototype is more than 10 centimeters in length, based on the agreement between numerical and experimental results with calculated Reynolds numbers consistent with the swimming conditions of micro organisms, the time-dependent model proves to be capable of real-time control studies [29], especially for future medical applications such as minimally invasive surgery.

It is experimentally and numerically confirmed that as the channel shrinks in diameter, the shear drag on the untethered robot increases and reduces its speed. The lowest velocity decrease is observed as 0.0653 mm/s for λ=10 mm and B_o = 3.5 mm, while the largest velocity drop occurs as 0.648 mm/s for λ=25 mm and B_o = 2.5 mm. It is also noted that 25% reduction in channel radius results in 38.9% decrease in the global average velocity of all body-tail assemblies.

Furthermore, contact friction calculations carried out by actuation system equations incorporated in RFT-model suggest that robot is in intermittent contact with the channel surface under the influence of other forces such as the weight and buoyancy as well as the induced flow field in the channel. It is noted that proposed model has the advantage of predicting effective friction without prior knowledge about the channel surface morphology with a single calibration.

Lastly, the effect of the geometric parameters of the helical tail, such as amplitude and wavelength, on the swimming speed and the body rotation rate is established by the experiments and models. SBT-based model provides accurate results in comparison to RFT-based model, whereas the latter is more flexible.

REFERENCES

[1] S. Martel, "Collective Methods of Propulsion and Steering for Untethered Microscale Nanorobots Navigating in the Human Vascular Network," *Journal of Mech. Eng. Science*, pp. 1505-1513, 2010.

[2] B. J. Nelson, I. K. Kaliakatsos, and J. J. Abbott, "Microrobots for Minimally Invasive Medicine," *Annu. Rev. Biomed. Eng.,* Vol. 12, pp. 55-85, April, 2010.

[3] R. Bogue, "The Development of Medical Microrobots: A Review of Progress," *Industrial Robot: An International Journal*, Vol. 35, No. 4, pp. 294-299, 2008.

[4] J. Edd, S. Payen, B. Rubinsky, M. L. Stoller, and M. Sitti, "Biomimetic Propulsion for a Swimming Surgical Micro-Robot," *IEEE/RSJ Intelligent Robotics and Systems Conference* (*IROS*), Vol. 3, pp. 2583-2588, Las Vegas, USA, October, 2003.

[5] T. Honda T, K. I. Arat, K. Ishiyama, "Micro swimming mechanisms propelled by external magnetic fields," *IEEE Trans. Magn.*, Vol. 32, No. 5, pp. 5085-5087, 1996.

[6] L. Zhang, J. J. Abbott, L. Dong, B. E. Kratochvil, D. Bell, and B. J. Nelson, "Artificial Bacterial Flagella: Fabrication and Magnetic Control," *Applied Physics Letters*, Vol. 94, pp. 064107-1-3, February, 2009.

[7] L. Zhang, K. E. Peyer, B. J. Nelson, "Artificial Bacterial Flagella for Micromanipulation," *Lab on a Chip*, Vol. 10, pp. 2203-22015, 2010.

[8] B. Chen, S. Jiang, Y. Liu, P. Yang, S. Chen, "Research on the Kinematic Properties of a Sperm-Like Swimming Micro Robot," *Journal of Bionic Engineering*, Vol. 7, Suppl., pp. S123-S129, 2010.

[9] K. E. Peyer, L. Zhang, B. E. Kratochvil, B. J. Nelson, "Non-Ideal Swimming of Artificial Bacterial Flagella Near a Surface," *IEEE International Conference on Robotics and Automation*, Anchorage, Alaska, May 2010.

[10] A. F. Tabak, F. Z. Temel, S. Yesilyurt, "Comparison on Experimental and Numerical Results for Helical Swimmers inside Channels," *IEEE/RSJ Intelligent Robotics and Systems Conference* (*IROS*), San Frascisco, USA, June 2011.

[11] A. W. Mahoney, J. C. Sarrazin, E. Bamberg, J. J. Abbott, "Velocity Control with Gravity Compensation for Magnetic Helical Microswimmers," *Advanced Robotics*, Vol. 25, pp. 1007-1028, 2011.

[12] E. M. Purcell, "Life at Low Reynolds Number," *American Journal of Physics*, Vol. 45, No. 1, pp. 3-11, 1977.

[13] E. Lauga, "Life Around the Scallop Theorem," *Soft Matter.*, Vol. 72, pp. 19-54, 2010.

[14] J. Gray, G. J. Hancock, "The Propulsion of Sea-Urchin Spermatozoa," *J. Exp. Biol.*, Vol. 32, pp. 802-814, 1955.

[15] C. Brennen, H. Winet, "Fluid Mechanics of Propulsion by Cilia and Flagella," *Ann. Rev. Fluid Mech.*, Vol. 9, pp. 339-398, 1977.

[16] J. Lighthill, "Flagellar hydrodynamics: The John von Neumann lecture," *SIAM Rev.*, Vol. 18, pp. 161-230, 1975.

[17] S. Chattopadhyay, X-L. Wu, "The Effect of Long-Range Hydrodynamic Interaction on the Swimming of a Single Bacterium," *Biophys. Journal*, Vol. 96, pp.2023-2028, 2009.

[18] J. J. L. Higdon, G. P. Muldowney, "Resistance Functions for Spherical Particles, Droplets and Bubbles in Cylindrical Channels," *J. Fluid Mech.,* Vol. 298, pp. 193-210, 1995.

[19] E. Lauga, W. R. DiLuzio, G. M. Whitesides, H. A. Stone, "Swimming in Circles: Motion of Bacteria Near Solid Boundaries," *Biophysical Journal*, Vol. 90, pp. 400-412, 2006.

[20] B. U. Felderhof, "Swimming at Low Reynolds Number of a Cylindrical Body in a Circular Tube," *Physics of Fluids*, Vol. 22, 113604, 2010.

[21] J. Happel, H. Brenner, *Low Reynolds Number Hydrodynamics*, N.J.: Prentice-Hall, Inc., 1965.

[22] E. Lauga, T. R. Powers, "The Hydrodynamics of Swimming Microorganisms," *Rep. Prog. Phys.*, Vol. 72, 096601, 2009.

[23] A. J. Hanson, H. Ma, "Visualizing Flow with Quaternion Frames," *Proc. of the conference on Visualization '94*, Washington, D.C., pp. 108-115, 1994.

[24] H. C. Berg HC, *Random walks in biology*, new expanded ed., USA: Princeton University Press, 1993.

[25] F. M. White, *Viscous fluid flow*, third ed., N.Y.: McGraw-Hill, New York, 2006.

[26] F. Perrin, "Mouvement Brownien d'un Ellipsoïde (I). Dispersion Diélectrique pour des Molecules Ellipsoïdales," *Le Journal de Physique et le Radium*, Série 7, Vol. 5, pp. 497-511, 1934.

[27] H. C. Berg, "The Rotary Motor of Bacterial Flagella," *Annu. Rev. Biochem.*, Vol. 72, pp. 19-54, 2003.

[28] M. W. Spong, M. Vidyasagar, *Robot Dynamics and Control*, USA: John Wiley & Sons, 1989.

[29] A. F. Tabak, S. Yesilyurt, "Experiment-Based Kinematic Validation of Numeric Modeling and Control of an Untethered Biomimetic Microrobot in Channel," *The 12th IEEE International Workshop on Advanced Motion Control* (*AMC2012*), Sarajevo, Bosnia and Herzegovina, March, 2012.

[30] L. F. Shampire, M. K. *Gordon, Computer Solution of Ordinary Differential Equations: The Initial Value Problem*, USA:Oxford University Press, 1985.